Measuring Light Yield with Isolated Protons in MicroBooNE

The MicroBooNE Collaboration

MICROBOONE-NOTE-1119-PUB,
Email: MICROBOONE_INFO@fnal.gov

Abstract

Liquid Argon Time Projection Chambers (LArTPCs) are precision detectors used extensively in neutrino physics. The MicroBooNE experiment at Fermilab is one of the experiments employing this technique and has collected 5 years of data from 2015-2021. The primary signal in LArTPCs is ionisation, but argon also emits large quantities of scintillation light, which can be used for calorimetry, timing and background rejection. Prompt scintillation light in MicroBooNE is recorded with an array of 32 PhotoMultiplier Tubes (PMTs). To enable the full use of scintillation light in the experiment, it is important to characterize the efficiency of light collection in the detector, i.e. the light yield. We present a new method of measuring the light yield using isolated proton interactions, which enables a position-dependent light yield measurement to map the response of the detector across its volume. This method can be used to calibrate the light response in large-scale LArTPC detectors as well as to test assumptions used in simulating scintillation light.

1 Introduction

The MicroBooNE experiment was built to study $O(1)$ GeV neutrino interactions from the Booster Neutrino Beamline (BNB). It also received an off-axis flux from the Main Injector (NuMI) beam [1]. The detector employed the Liquid Argon Time Projection Chamber (LArTPC) detector technology to obtain high resolution images which allowed the detection and identification of different neutrino-interaction final-state particles with a low energy threshold. The high resolution images are created by recording the three-dimensional pattern of ionised charge produced from charged particles with a mm accuracy. However, the slow (ms-scale) drift of electrons washes out the μs resolution of BNB's beam structure. The scintillation light, produced abundantly together with ionised electrons, propagates through the detector volume in nanoseconds and can be used to recover the timing information once it is correctly associated to the ionisation signals. To fully exploit this capability, a better understanding of the light propagation and detection efficiency is necessary.

For this analysis we define the light yield to be the amount of light detected per unit of deposited energy. It is expected to vary as a function of position in the detector. Additionally, the amount of scintillation light emitted can be affected by quenching which is caused by impurities in LAr, such as nitrogen, oxygen and water. Studies show that the quenching will become impactful when the concentration is above $\mathcal{O}$(1 ppm) for Nitrogen and $\mathcal{O}$(0.1 ppm) for Oxygen [2]. The light propagation can be influenced by absorption, reflections and Rayleigh scattering, where this last effect occurs when a photon scatters with a nucleus elastically and coherently. With these considerations, there is a strong need for point-like sources to enable a precise mapping of the light detection capability in the detector. Isolated protons can be regarded as "point-like" sources and thus are good candidates to perform the measurement of the light yield.

2 The MicroBooNE detector

MicroBooNE was a LArTPC detector running at Fermilab from 2015 to 2021. It acquired 1.56×10^{21} Protons On Target (POT) BNB data and 2.37×10^{21} POT NuMI data during its run. The active part comprised of a TPC of the size of 10.4 m $\times$ 2.3 m $\times$ 2.5 m, resulting in an active mass of 87 tonnes. Details about the construction and operation of MicroBooNE can be found in [3].

2.1 The coordinate system

MicroBooNE uses a right-handed Cartesian coordinate system in which x, y and z denote the drift, vertical and beam-aligned direction. The origin is defined to be located centred in the vertical direction, on the first induction plane near the anode, and on the upstream face of the LArTPC [3]. Figure 1 shows the coordinate system and boundaries of MicroBooNE with a cartoon.

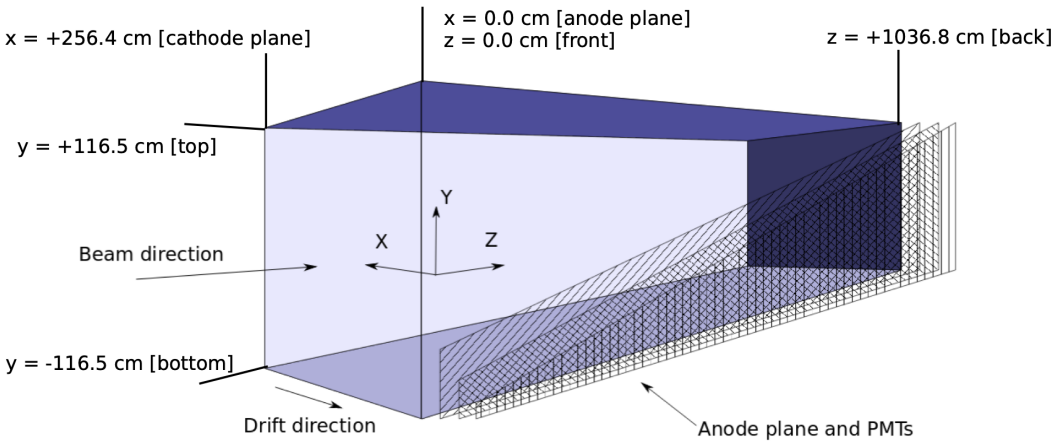

Figure 1: A depiction of the coordinate system for MicroBooNE [4].

2.2 The light detection system

MicroBooNE's primary light detection system consists of 32 8" diameter Hamamatsu R5912-02mod cryogenic PMT behind a TPB-coated acrylic plate and inside a mu-metal shield [3]. Their position in the YZ plane is marked by the circles in Figure 2. The TPB is used to shift the 128 nm wavelength emitted in argon to the visible region which is the sensitive region of the PMTs. The cryogenic PMTs are operated with high voltage of about 1300 V. The PMT gain is defined in units of charge recorded per photo electron (PE), and needs to be re-calibrated with minor adjustments to the HV every time the PMT system restarts [5]. The light detection system is located in the $y-z$ plane behind the anode planes of the LArTPC. Each PMT detects optical hits, and those with the same arrival time within one event are further clustered into flashes. During the summer accelerator shutdown period after Run 2, one PMT stopped working due to a faulty connection [5]. Additionally, two PMTs with an electronics response different from nominal are not used in this analysis. These two PMTs are however used in MicroBooNE analyses, accounting for their specific signal response.

2.3 Optical reconstruction

Pulse-finding algorithms are applied to digitized waveforms. The collection window is defined with the slow component of Ar scintillation light around 8 μs. Recorded light pulses within this window are referred to as in-time pulses and are reconstructed as optical hits. The in-time hits from all photosensors are clustered into optical flashes that represent the light of a particle interaction in the detector.

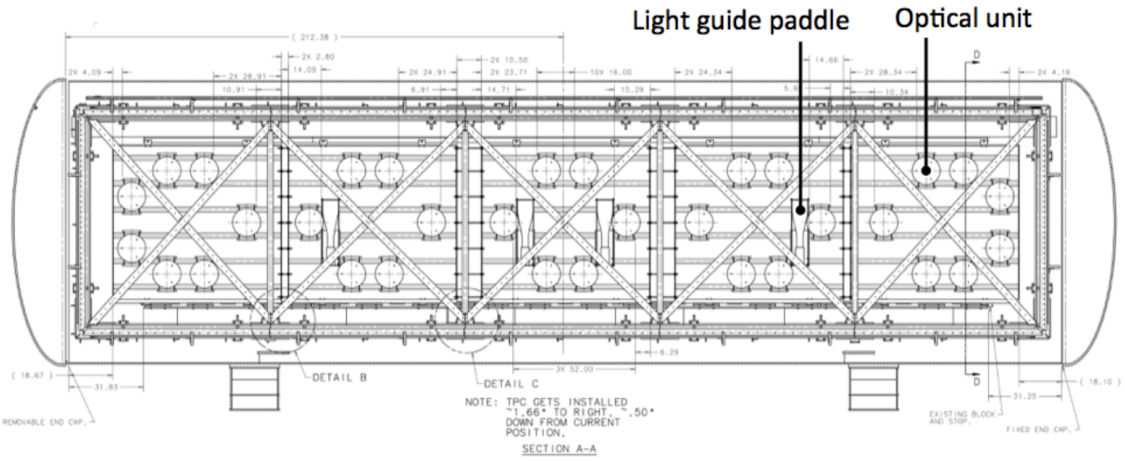

Figure 2: The MicroBooNE light collection system, which is mounted behind the anode wire planes. Figure from [3].

3 Data sample

A sample of cosmic-ray isolated protons is acquired by identifying events from MicroBooNE off-beam cosmic data with an interaction in the TPC which is in-time with the unbiased PMT readout window [6]. Pandora's TPC pattern-recognition reconstruction [7] is used to identify isolated interactions in each event, and MicroBooNE's flash-matching algorithms [8] are further applied to isolate interactions in-time with the unbiased PMT readout window. The entirety of MicroBooNE's off-beam dataset from the first three years of data-taking is leveraged for the analysis. Figure 3 shows a distribution of the particle ID (PID) score [9] for events with track-like particles for MicroBooNE's on and off-beam datasets. PID scores of -1 are associated with proton-like tracks. While multiple categories of events contribute to the distribution, the zoom-in on the right shows the contribution from off-beam data specifically in the range [-1, 0] which is dominated by proton-like tracks. For this off-beam sample a clear peak of proton-like events is observed, indicating the presence of many proton-like tracks in off-beam data, which can be leveraged for the analysis. The pre-selection cut for PID score is tailored to isolate protons and set to be -0.3. Figure 4 shows an example of PMT waveforms from a proton candidate.

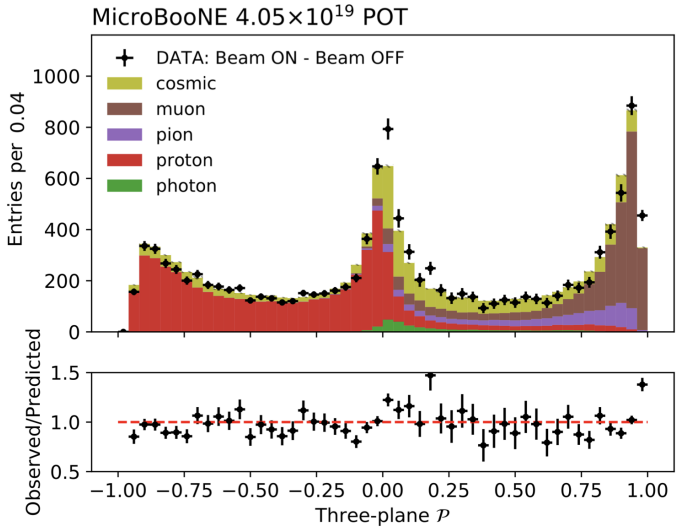

Figure 3: The distribution of the particle ID score for events with track-like particles for MicroBooNE's full (left) and off-beam only (right) datasets. The EXT on the left represents the off-beam dataset [10].

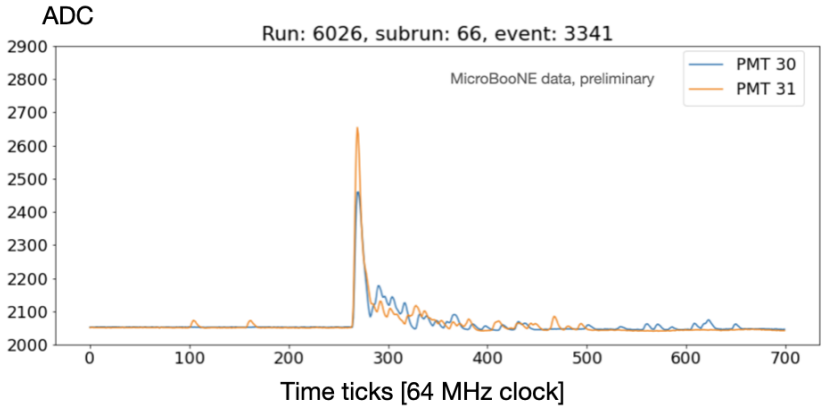

Figure 4: An example of PMT waveforms from a proton candidate in data.

4 Event selection

Example events passing the pre-selection cut are shown in Figure 5. A reconstructed proton track is displayed on the left of Figure 5. For some events where either the track crosses the border of the detector or the track length is too long, as shown in the middle and the right of Figure 5, separately.

The goal of this analysis is to select point-like isolated proton events throughout the detector, excluding the events seen in the middle and the right plots of Figure 5. Using the TPC topological information, we first remove the tracks with lengths above 30 cm and require the reconstructed vertex and endpoint positions associated with proton candidates to be within

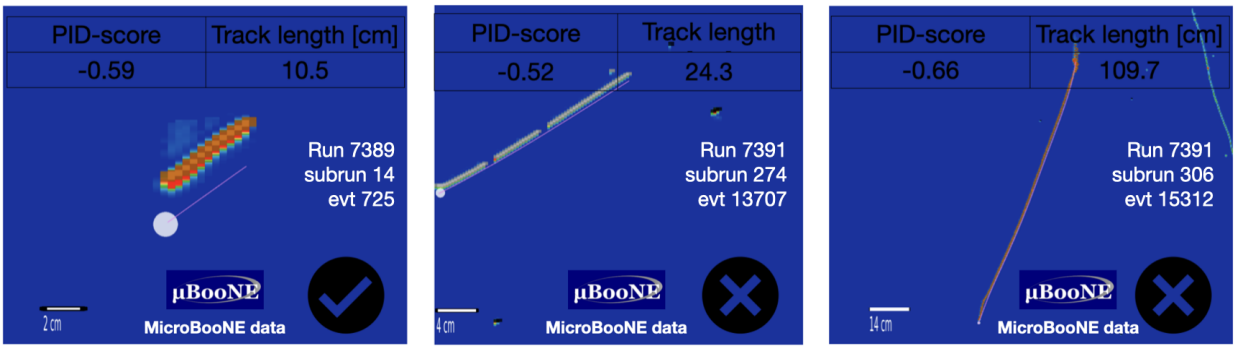

Figure 5: Event displays of three candidate tracks after preselection.

the fiducial volume. For the latter cut, we employ additional constraints to ensure the events avoid cutting through voxels, which are the unit regions of the optical-library based detector simulation. We choose 12.375 cm from the border of the active volume in the x-axis, 10.49 cm in the y-axis, and 11.5941 cm in the z-axis. Then since we expect the light yield to vary strongly as a function of drift distance, this component of the track, denoted as "x", is limited to be smaller than 10 cm. In addition to this cut, we further require that the tracks we use remain in one bin with width of 30 cm along the drift direction to ensure that the photons produced by these tracks do not contribute to multiple bins.

Light reconstruction quality cuts are also applied for selections. The distances between the reconstructed light flash centres and the midpoints of tracks are required to be smaller than the flash width in the z-direction to confirm that photons are generated from the reconstructed tracks. Due to the limited row numbers in PMT layouts, as drawn in Figure 2, the similar cut is not applied in the y-direction. We also request a cut of 160 cm on the distance between midpoints of tracks and flash centres in the $y-z$ plane to remove additional mis-matched events. After the series of selection cuts, there are 595 proton candidates (out of 49257 in-time candidates) in Run 1 off-beam data, 1856 candidates (out of 150347 in-time candidates) in Run 3 off-beam data. The difference in statistics is mainly due to having collected more Run3 off-beam data. Figure 6 shows the distributions of midpoints in x, y and z directions for selected proton candidate tracks. As expected, it covers the whole range along the x direction, and a higher distribution is observed with higher y because our sample comes from cosmic rays. The z-direction, the dips in small z and around 700 cm are due to the difficulty to reconstruct "point-like" tracks in a region of the collection-plane with unresponsive wires [11].

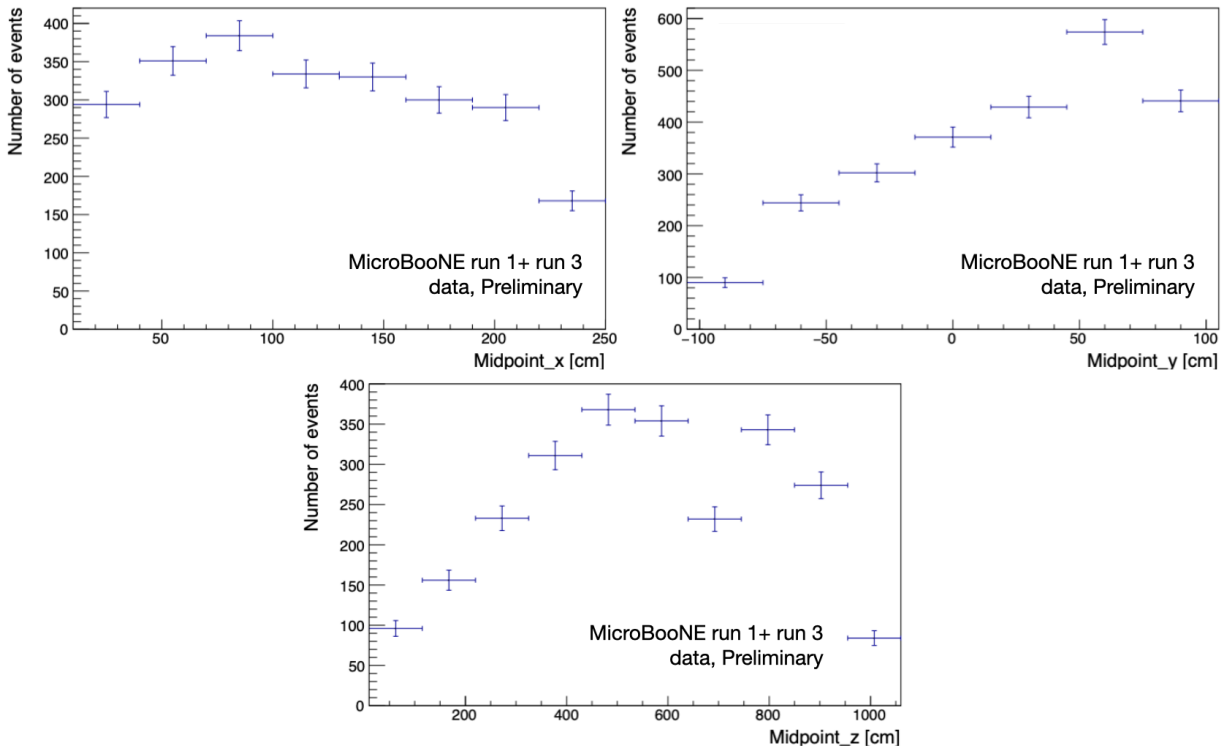

Figure 6: Top left: the distributions of proton candidate midpoints in x-direction. Top right: the distributions of proton candidate midpoints in y-direction. Bottom: the distributions of proton candidate midpoints in z-direction

5 Total light yield measurement

5.1 Total light yield along the drift direction

With a clean sample of protons after selections, the position-dependent total light yield can be measured. The total light yield is calculated by dividing the number of reconstructed photon candidates in the flashes by the energy deposited by the protons and then compared with simulation. The simulation utilise a semi-analytical model assuming different Rayleigh scattering lengths [12], 60 cm and 100 cm respectively. This simulation is not used by default in MicroBooNE, but comparable results can be obtained. The total light yield with the drift direction with run 1 data only is plotted in Figure 7, while with both run 1 and run 3 data is plotted in the upper plot of Figure 8. The ratio between run 3 and run 1 data is shown in the lower plot of Figure 8. The uncertainties for data and simulations are using error on the mean. Since we aims to measure the light yield, the O(20%) uncertainty on the light yield used by MicroBooNE for other analyses [13] are not plotted in this analysis.

From Figure 8, we see that the simulated light yield with two Rayleigh scattering lengths are quite similar in MicroBooNE. The light yield is not uniform along the drift direction, and decreases rapidly when increasing the drift distance. Due to the light-yield decline during the run 2 period, the light-yield of run 3 is much smaller than run 1 [13]. Moreover,

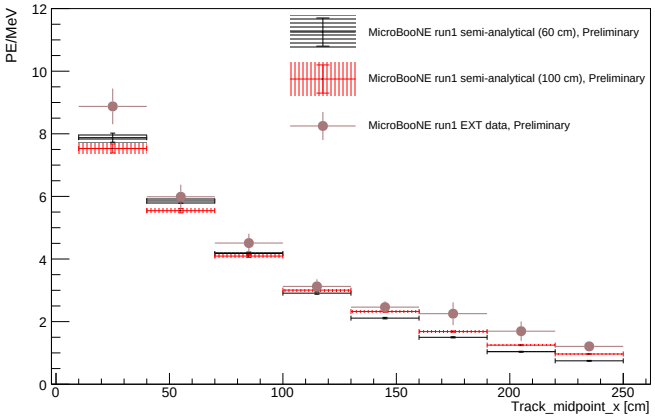

Figure 7: Total light yield measured as a function of drift distances. Data is compared with simulations from the semi-analytical model with different Rayleigh scattering lengths, run 1 only.

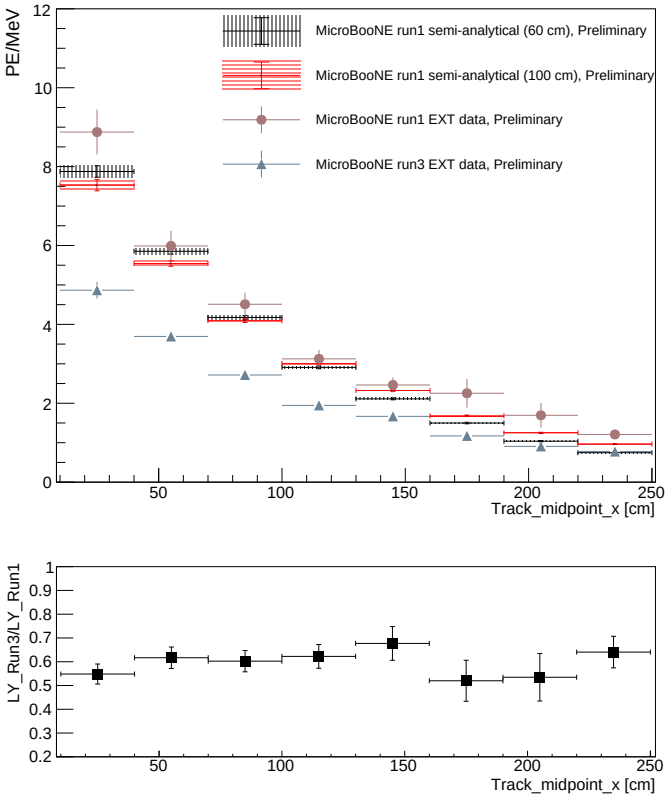

Figure 8: Top: total light yield measured as a function of drift distances. Data is compared with simulations from the semi-analytical model with different Rayleigh scattering lengths. Bottom: the ratio of total light yield in run 3 data to these in run 1 data.

the ratio between the total light yield in Run 3 and Run 1 is mostly flat around 0.6 with some fluctuations. Data results show a slight excess over simulations in the lowest x-bin, possibly related to the challenge in simulating the light response at high off-set angles between scintillation points and photon detectors.

To study this, a set of plots describing total light yield varying in the $y-z$ plane with different drift distances are generated. An example is shown in Figure 9-left for protons in the [10,40] cm range. We find that in the low-x half of the detector, due to the variation of off-set angles, the light yield changes drastically across the $y-z$ plane. Thus we apply an additional hexagonal cut to only select events in line with PMT arrays when $x < 70$ cm, as shown on the right of Figure 9.

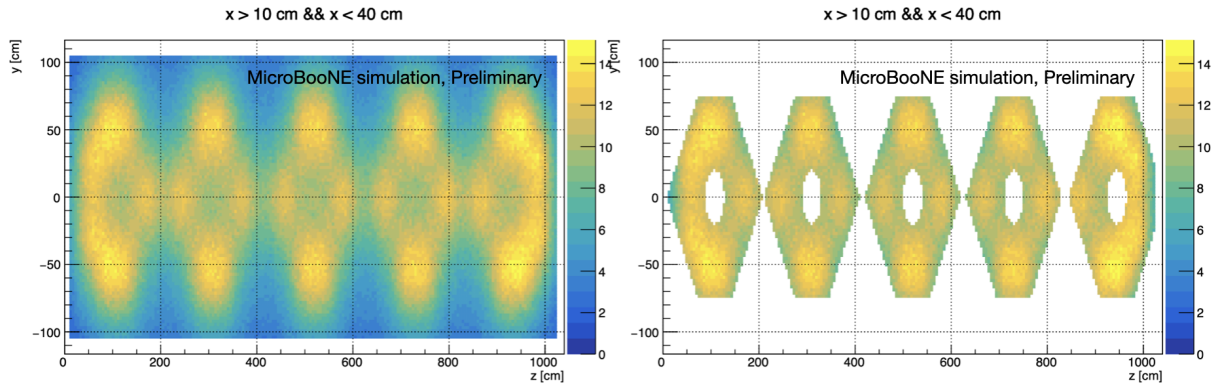

Figure 9: Left: The total light yield map in $y-z$ plane for $10 < x < 40$ cm before selections. Right: The selected total light yield map in $y-z$ plane for $10 < x < 40$ cm where scintillation points are in-line with PMTs .

With the hexagonal cut, the total light yield along drift direction is plotted in Figure 11, while run 1 only is shown in Figure 10. Both simulations and data are seeing more light as expected, and simulations show a good agreement with data.

5.2 Total light yield in the vertical/beam direction

The data enables us to calculate the light yield in the vertical and beam directions as well. In the vertical direction shown in Figure 12 and Figure 13, the light yield is higher in the middle part of the detector compared to the light yield at the top and bottom. This is mainly due to the border effect caused by the absorption from the wall of the detector. As for along the beam direction, both predicted and detected light yields are almost uniform, as plotted in Figure 14 and Figure 15. The dip in Run 1 in the first two bin in z-direction is caused by the absence of the two removed PMTs, as described in Section 2.2. This effect is somewhat cancelled in run 3 due to a statistical fluctuation resulting in a larger contribution of events with smaller drift distances. The border effect in the largest z-bin is not observed. This is because the effect seen by border PMTs is washed out by the inner PMTs which belong to same z bin.

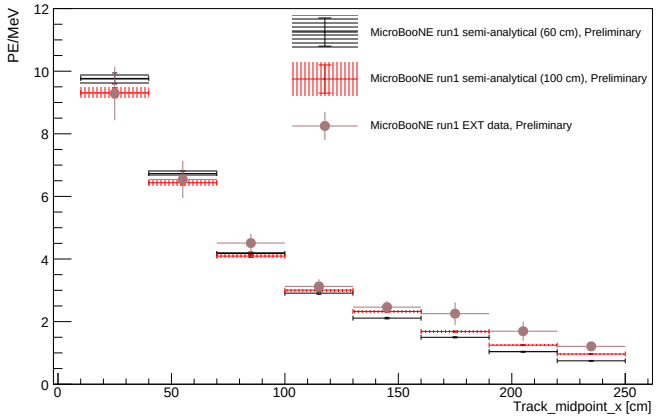

Figure 10: Total light yield measured as a function of drift distances with the hexagonal cut. Data is compared with simulations from semi-analytical model with the different Rayleigh scattering lengths, run 1 only.

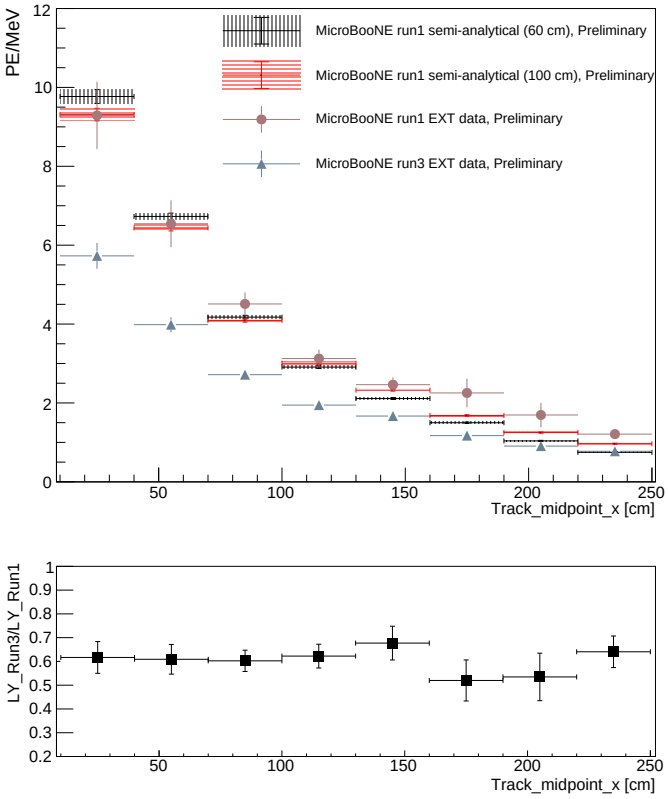

Figure 11: Top: total light yield with regard to different drift distances with the hexagonal cut. Data is compared with simulations from semi-analytical model with the different Rayleigh scattering lengths. Bottom: the ratio of total light yield in run 3 data to these in run 1 data with the hexagonal cut.

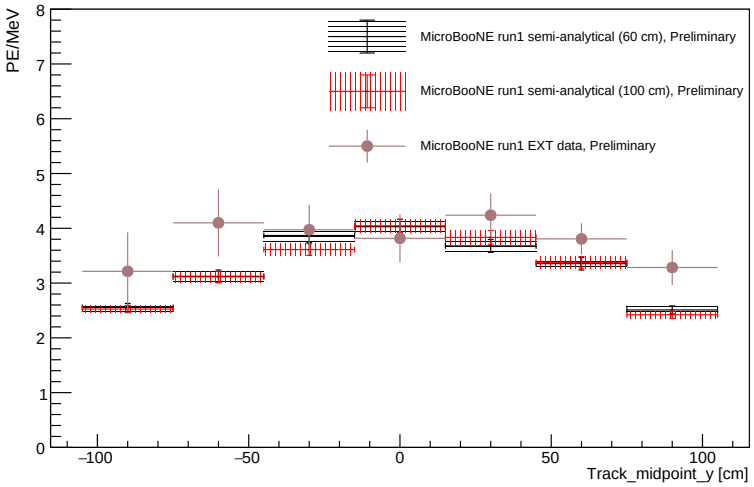

Figure 12: Total light yield with different positions in the vertical direction. Data is compared with simulations from semi-analytical model with different Rayleigh scattering lengths, run 1 only.

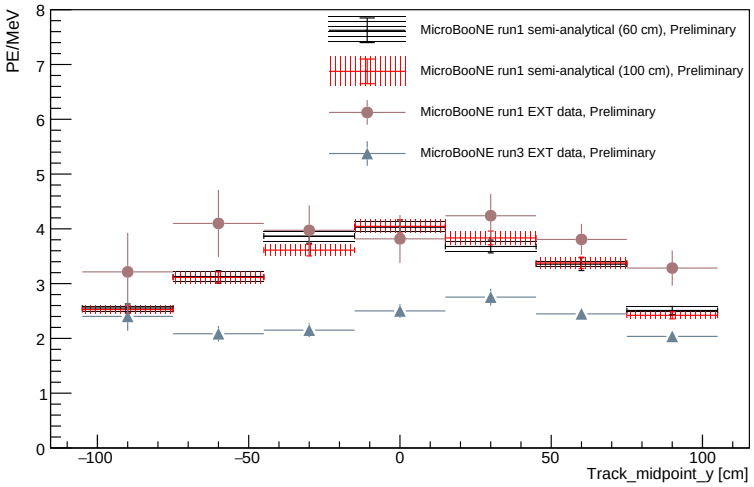

Figure 13: Total light yield with different positions in the vertical direction. Data is compared with simulations from semi-analytical model with different Rayleigh scattering lengths.

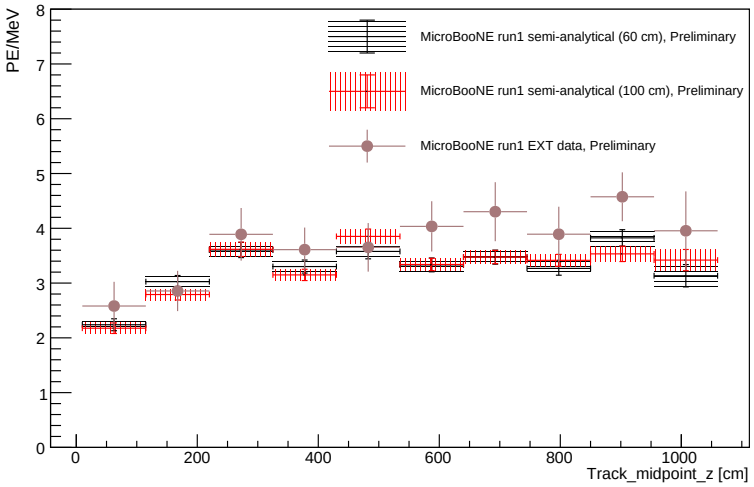

Figure 14: Total light yield with different positions in the beam direction. Data is compared with simulations from semi-analytical model with different Rayleigh scattering lengths, run 1 only.

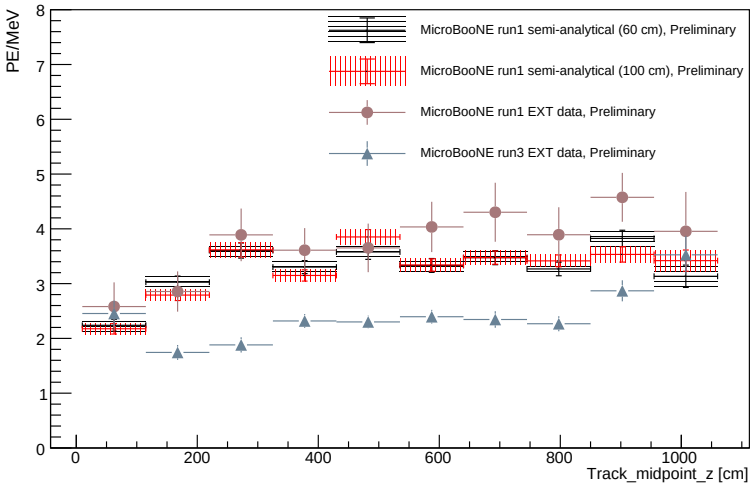

Figure 15: Total light yield with different positions in the beam direction. Data is compared with simulations from semi-analytical model with different Rayleigh scattering lengths.

6 PMT-by-PMT measurement

The total light yield study shows that it is challenging to measure the light response as a function of drift-distance alone because the total light yield versus drift distance can be significantly influenced by different positions in the $y-z$ plane in small x, while the total light yield against vertical and beam direction can be influenced if there is a high density of events with smaller x in one bin. Thus to study the distance dependence more accurately, we define a new variable for the analysis: the absolute distance between the midpoint of a track to each PMT. To suit this purpose, the number of detected photons is separated by each PMT, enabling a PMT-by-PMT measurement. This results in an effective increase of the number of measurements (one per PMT) and therefore the sample statistics. The result of light yield of a single PMT changing with different absolute distances is shown in Figure 17. The run 1 only plot is in Figure 16. As expected, the light yield also decreases significantly with increasing absolute distances, analogously to the measurement in the drift direction. Furthermore, we show that by using the full 3D distance, the light yield dependence can be studied more precisely.

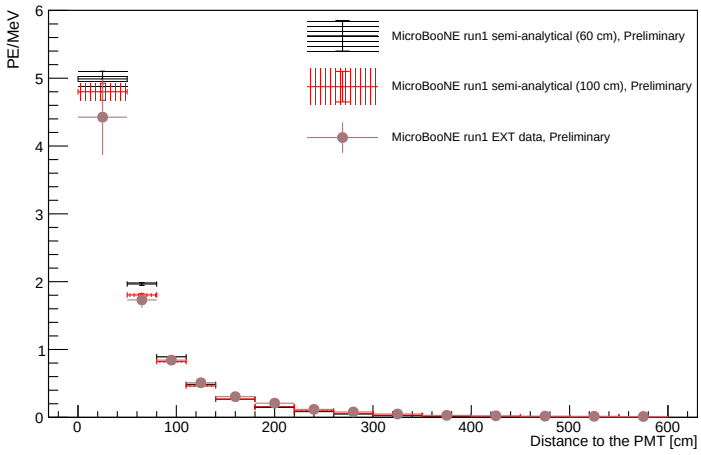

Figure 16: Light yield measured as a function of the distance to the PMT. Data is compared with simulations from the semi-analytical model with different Rayleigh scattering lengths, run 1 only.

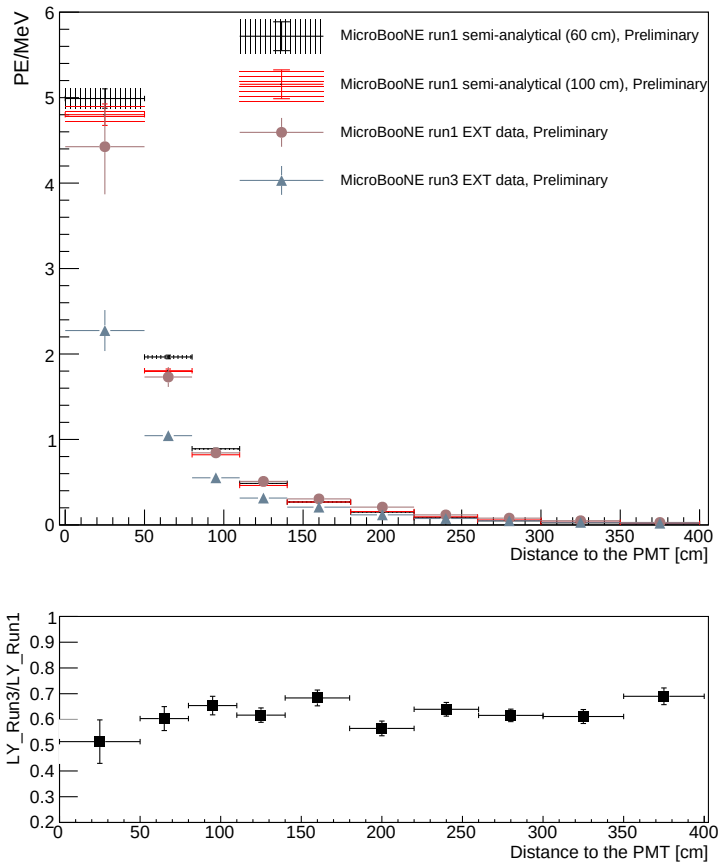

Figure 17: Top: light yield measured as a function of the distance to the PMT. Data is compared with simulations from the semi-analytical model with different Rayleigh scattering lengths. Bottom: the ratio of light yield in run 3 data to these in run 1 data.

7 Conclusion

In this note, we present a new method of measuring the light yield using isolated proton events from cosmic rays in the MicroBooNE detector. This enables a position-dependent light yield measurement to map the response of the detector across its volume. From the present results, we confirm a decline from run 1 to run 3, which agrees with the previous study. Moreover, the decline is independent of detector coordinates, which is consistent with the calibration applied in MicroBooNE simulation and reconstruction. We also show that the data overall are well modeled by the simulation. As expected given the configuration of MicroBooNE's light detection system, the light yield decreases significantly as a function of the drift-distance, while it remains relatively steady along the beam direction, and the light yield is higher in the middle of the detector compared to the top and the bottom. We discuss the pitfalls of using the drift-distance, which leads to the PMT-by-PMT measurement where the 3d distance is introduced in this analysis. The light yield with increasing distance also decreases as expected. This method can be used to calibrate the light response in large-scale LArTPC detectors as well as to test assumptions used in simulating scintillation light.

References

[1] P. Adamson et al. The NuMI Neutrino Beam. *Nucl. Instrum. Meth. A*, 806:279–306, 2016. doi: 10.1016/j.nima.2015.08.063.

[2] R. Acciarri et al. Effects of nitrogen and oxygen contaminations in liquid argon. *Nuclear Instruments & Methods in Physics Research Section a-Accelerators Spectrometers Detectors and Associated Equipment*, 607:169–172, 08 2009. doi: 10.1016/j.nima.2009.03.142.

[3] R. Acciarri et al. Design and construction of the microboone detector. *Journal of Instrumentation*, 12(02):P02017–P02017, Feb 2017. ISSN 1748-0221. doi: 10.1088/1748-0221/12/02/p02017. URL `http://dx.doi.org/10.1088/1748-0221/12/02/P02017`.

[4] The MicroBooNE Collaboration. Establishing a pure sample of side-piercing through-going cosmic-ray muons for lartpc calibration in MicroBooNE. . URL `https://microboone.fnal.gov/wp-content/uploads/MICROBOONE-NOTE-1028-PUB.pdf`. MICROBOONE-NOTE-1028-PUB.

[5] The MicroBooNE Collaboration. PMT gain calibration in MicroBooNE. . URL `https://microboone.fnal.gov/wp-content/uploads/MICROBOONE-NOTE-1064-TECH.pdf`. MICROBOONE-NOTE-1064-TECH.

[6] D Kaleko. PMT triggering and readout for the MicroBooNE experiment. *Journal of Instrumentation*, 8(09):C09009–C09009, sep 2013. doi: 10.1088/1748-0221/8/09/c09009. URL `https://doi.org/10.1088/1748-0221/8/09/c09009`.

[7] R. Acciarri et al. The Pandora multi-algorithm approach to automated pattern recognition of cosmic-ray muon and neutrino events in the MicroBooNE detector. *Eur. Phys. J. C*, 2017. URL `https://cds.cern.ch/record/2286065`.

[8] Wouter Van De Pontseele. Flash-Matching for the ν_e Selection in MicroBooNE. In *Prospects in Neutrino Physics*, pages 179–183, 5 2018.

[9] Polina Abratenko et al. Calorimetric classification of track-like signatures in liquid argon tpcs using microboone data. *Journal of High Energy Physics*, 2021, 12 2021. doi: 10.1007/JHEP12(2021)153.

[10] Polina Abratenko et al. Calorimetric classification of track-like signatures in liquid argon tpcs using microboone data. *Journal of High Energy Physics*, 2021, 12 2021. doi: 10.1007/JHEP12(2021)153.

[11] R. Acciarri et al. Noise characterization and filtering in the MicroBooNE liquid argon TPC. *Journal of Instrumentation*, 12(08):P08003–P08003, aug 2017. doi: 10.1088/1748-0221/12/08/p08003. URL `https://doi.org/10.1088/1748-0221/12/08/p08003`.

[12] Diego Garcia-Gamez et al. Predicting Transport Effects of Scintillation Light Signals in Large-Scale Liquid Argon Detectors. *Eur. Phys. J. C*, 81(4):349, 2021. doi: 10.1140/epjc/s10052-021-09119-3.

[13] The MicroBooNE Collaboration. Light yield calibration in MicroBooNE. . URL https://microboone.fnal.gov/wp-content/uploads/MICROBOONE-NOTE-1120-TECH.pdf. MICROBOONE-NOTE-1120-TECH.